

Compact Evanescent Optical Switch and Attenuator with Electromechanical Actuation

Franck Chollet, M. de Labachellerie, and Hiroyuki Fujita, *Member, IEEE*

Abstract— We report the design and the realization of an out-of-plane bending structure supporting a waveguide that is used as an optical attenuator and an optical switch. Both devices are based on evanescent field interaction induced by spatial confinement either between two waveguides or between one waveguide and an absorbing medium. The attenuator exhibits typical attenuation of 65 dB/cm. Even if the bad quality of the waveguide has prevented the correct operation of the switch, we show that the attenuation figure establishes the feasibility of a compact evanescent optical coupler with mechanical drive featuring a total length below 1 mm.

Index Terms— Electrostatic actuator, MEMS, optical attenuator, optical switch.

I. INTRODUCTION

THE optical microelectromechanical systems (MEOMS or MOMS) are foreseen to provide low-cost devices for the telecommunications. They have the unique property to allow the batch processing of device based on simple bulk optic principles. For example, the fiber-based MOMS switches use the reflection of the beam on a small moving mirror [1], [2] or the displacement of an input fiber between two output fibers to achieve wavelength- and polarization-independent operation [3]. Another approach uses waveguides instead of fibers. The MEMS technology permits to combine the advantages of the mechanical switches (low loss, low crosstalk) with the compactness of the integrated optics devices. Some waveguide-based MOMS switches have already been proposed relying either on spoiled total reflection [4], [5], on moving waveguides [6], [7], or on evanescent coupling. In the last case, two coupled waveguides are perturbed to spoil the phase-matched condition which ensures the coupling. This effect is obtained by bringing a dielectric [8] or a metallic membrane [9] into contact with one of the waveguide. Our approach to this problem is to induce an evanescent coupling between two superimposed, or stacked, waveguides by narrowing the gap between them. We call this principle of operation, the space-driven evanescent coupling in contrast to the index-

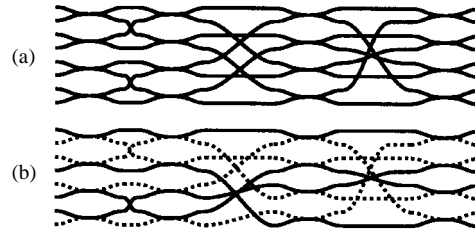


Fig. 1. Top-view of an 8×8 optical switch matrix with (a) a conventional planar structure and (b) a two-level structure (full line and dotted line represents the waveguides on the upper and lower level, respectively).

driven coupling of the previous devices. The foreseeable benefits of our approach is its ability to yield very compact devices, smaller by at least one order of magnitude than existing integrated optic switches, with a very high ON-OFF contrast. Moreover, this principle yields 2×2 symmetrical switch that may be used for an $N \times N$ optical switch, a possibility that is not allowed by many of the other 1×2 waveguide switches [3], [6], [7]. The nonplanar topology of the device has the advantage over a conventional planar design to suppress the patterning of Y -branches that often introduce additional loss. The Y -branches are created by the bending of the waveguide. Moreover, we can see in Fig. 1 that it lowers the number of waveguide crossing (in this case from 20 to 14), decreasing further the expected loss. A more detailed study of the characteristics of this two-level architecture will be published later.

In the first part, we introduce the principle of operation of the device as a coupler or an attenuator. Then, we discuss a theoretical model that allows for the device design according to expected performances. The third part is devoted to the device realization through a silicon-based process. Eventually, we exhibit optical results obtained with the device used as an attenuator that confirm the feasibility of the space-driven evanescent coupler.

II. PRINCIPLE OF OPERATION

The device is based on the evanescent coupling that appears between two waveguides when the gap between them is narrowed. In the through state [Fig. 2(a)], as no external force is applied, the two superimposed waveguides are isolated by a low-index gap to prevent the optical signal to go from one waveguide to the other. In the crossover state [Fig. 2(b)], the upper waveguide bends down and the gap is narrowed. The evanescent coupling appears and after propagation of a char-

Manuscript received June 8, 1998; revised September 23, 1998. This work was supported in part by the Japan Society for the Promotion of Science.

F. Chollet was with LIMMS/CNRS-IIS, University of Tokyo, Minato-ku, Tokyo 106, Japan. He is now with the IMRE, National University of Singapore, Singapore 119260, Singapore.

M. de Labachellerie is with LPMO/CNRS-IMFC, Université de Franche-Comté, 25030 Besançon cedex, France.

H. Fujita is with LIMMS/CNRS-IIS, University of Tokyo, Minato-ku, Tokyo 106, Japan.

Publisher Item Identifier S 1077-260X(99)00641-3.

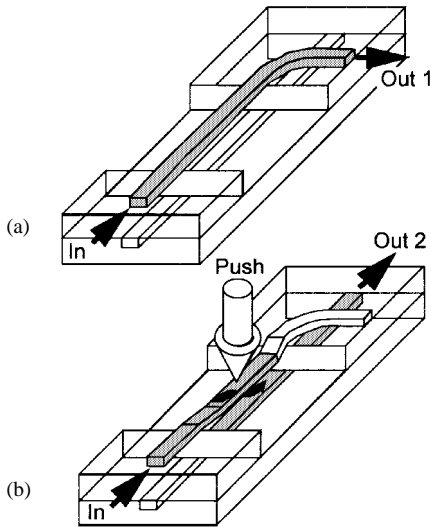


Fig. 2. Operation of the space driven evanescent coupler in (a) the through state and (b) the crossover state.

acteristic distance, known as the coupling length, the signals carried by the two waveguides are exchanged. The advantage of this architecture compared with the conventional electro-optic devices is in the large change in coupling efficiency that is obtained between the two states of the device. The small variations of efficiency achievable through the electrooptic effect require using centimeter-long interaction region. We will see that our device reduces the active length by at least one order of magnitude.

In order to obtain optical attenuation the upper waveguide is replaced by a layer that absorbs light [10], [11]. In the crossover state, the light coupled in the layer will be absorbed in a very short distance. This distance depends heavily on the choice of the absorbing material.

Clearly, in order to get compact devices, we need a high intensity of the evanescent field inside the low-index gap and this gap should be very small in the crossover state. The first requirement decides the choice of the waveguide while the latter dictates the characteristics of the actuator.

III. OPTICAL MODEL

From the above principle of operation we understand that the optical behavior impose strict conditions on the actuator design. However, an optomechanical coupled model is not needed and we will study separately these two aspects of the device, beginning with the optical behavior.

A. Coupler

Coupling between two waveguides is usually described [12] using the weak coupling approximation by a set of coupled equations relating the slowly varying amplitude of the two coupled modes, $a(z)$ and $b(z)$. Solving these equations with two waveguides separated by a low index gap and with relevant boundary conditions yields (1) that relates the intensity transported by the two modes, I_a and I_b , with the

propagation distance z

$$\begin{aligned} I_a(z) &= a(z)a^*(z) \\ &= I_a(0) \left[\cos^2 \left(\sqrt{\kappa^2 + \delta^2} z \right) \right. \\ &\quad \left. + \frac{\delta^2}{\kappa^2 + \delta^2} \sin^2 \left(\sqrt{\kappa^2 + \delta^2} z \right) \right] \\ I_b(z) &= b(z)b^*(z) \\ &= I_a(0) \frac{\kappa^2}{\kappa^2 + \delta^2} \sin^2 \left(\sqrt{\kappa^2 + \delta^2} z \right) \end{aligned} \quad (1)$$

where κ is the coupling coefficient and 2δ the difference between the propagation constants of the two modes. The power in the second waveguide reveals the existence of a periodic exchange of signal between the two waveguides. The period is twice the coupling length, L_C , which is given by

$$L_C = \frac{\pi}{2\sqrt{\kappa^2 + \delta^2}}. \quad (2)$$

This relation is governed by the coupling coefficient, κ , which is proportional to the overlap between the two fields of the modes excited in the waveguides:

$$\kappa \propto \iint_{\text{core}} u(x, y)u(x + g + h, y) dx dy \quad (3)$$

where $u(x, y)$ is the lateral profile of the mode, g the gap width, and h the thickness of the waveguide core. The previous equations are essentially valid for both TE and TM polarization. However, there is a small difference in the coupling coefficient for the two polarizations that will translate in coupling length difference of several percents. Thus, we will observe slightly different coupling efficiencies for the two modes at the end of the coupler but essentially the device will be polarization insensitive if not independent [13]. In order to obtain short coupling length, we have to achieve the largest possible ratio between the power flowing outside the core, which may excite the mode in the other waveguide, and the total transported power. Because the evanescent field decreases much less in the high index fluid than in the air, a simple way to increase this ratio is to fill the gap between the two waveguides with a matching index fluid. Another way, is to use specially designed waveguides which intrinsically possess the ability to carry an important part of the power in the evanescent part of the field. Thus in order to further evaluate these possibilities, we first compute with finite element method (FEM) the optical field of the fundamental modes of different waveguides. Then, we use (3) to plot the variation of the coupling length with the gap width. In order to calculate the proportionality constant we computed the coupling length for an $0.2 \mu\text{m}$ -wide air gap with a scalar 3D-BPM program (BPMCAD).

Fig. 3 shows the result of the simulation for two identical SiON rib waveguides with a core $1.5 \mu\text{m}$ -wide, $0.8 \mu\text{m}$ -thick, and with a refractive index $n = 1.510$, on a SiO₂ substrate ($n = 1.454$) (bent part is described by the flexion of a fixed-end/guided-end beam under local load [14]). Complete coupling (100%) is obtained after $200 \mu\text{m}$ of ‘‘contact’’ zone with the $0.2 \mu\text{m}$ -wide air-gap. We also ran the 3D-BPM

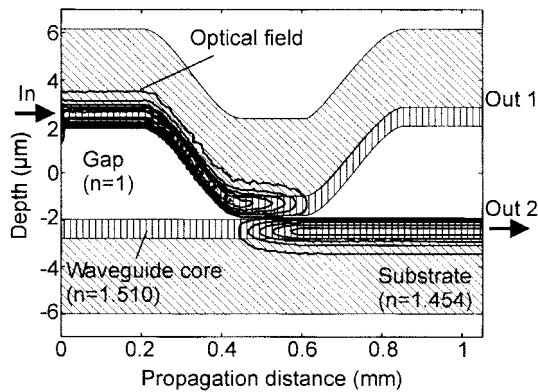


Fig. 3. BPM simulation showing the intensity of light along the waveguides in Fig. 2(b) with $\lambda = 0.6 \mu\text{m}$.

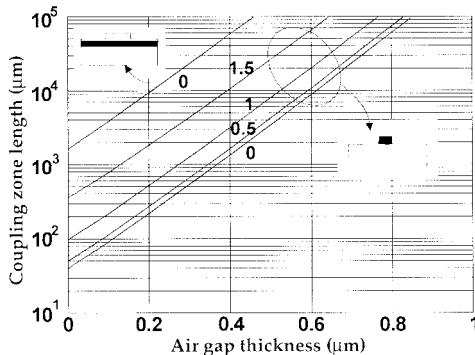


Fig. 4. Coupling length versus the air gap thickness and the misalignment for two types of waveguide at $\lambda = 0.6 \mu\text{m}$ (the label of the curves gives the lateral misalignment between the two waveguides in μm).

simulation for a few other thickness and refractive indices of the material filling the gap in order to validate the method. A good agreement between the overlap calculus and the BPM simulation has been observed as the index of the material filling the gap was sufficiently far from the index of the core. This condition insures that the field in each waveguide is not too much perturbed by the presence of the other waveguide. With this procedure we avoid the time consuming 3D-BPM calculus and we may also include the effect of lateral misalignment. Fig. 4 presents curves for two types of singlemode waveguides: a rib waveguide (etched core) and a strip-loaded waveguide (etched superstrate).

The coupling length increases exponentially with the gap thickness, which is consistent with the expected exponential decrease of the optical field outside the core. Thus an important parameter to determine the device length is the minimum gap that may be obtained when the two waveguides are brought into contact. We have measured with a stylus profilometer the surface roughness of the typical waveguide layer stack. We observed a maximum roughness around $0.1 \mu\text{m}$, with a very good reproducibility along runs. Therefore, it seems reasonable to state on a minimal gap around $0.2 \mu\text{m}$ for the device if the flatness of the structure is otherwise guaranteed. It is apparent in Fig. 4 that the lateral misalignment modifies rapidly the coupling length of the device. A tilt between the two waveguides also tends to increase the coupling length and to suppress the periodic exchange of power [15]. Therefore, the misalignment

of the two waveguides has to be kept below $0.5 \mu\text{m}$. We also observe in Fig. 4 that the strip-loaded waveguide has much longer coupling length because the attenuation experienced by the optical field inside the superstrate decreased drastically the magnitude of the evanescent field. It seems that for the realization of compact device a rib waveguide is the best choice. It presents the further advantage to allow the design of sharp bends without excessive loss, because of the large index difference existing between the core and the cladding. This point is of particular interest for the compact implementation of large commutation matrix. As we mentioned before, another way to reduce the length of the coupler is to introduce a fluid between the two waveguides that will decrease the optical index mismatch existing between the waveguide and the medium in the gap. We have estimated this effect using the expression of the optical field outside the core in a planar waveguide [16]. We assume that the propagation constant is not changed by the presence of the material in the gap and we find the proportionality constant from Fig. 3, where air ($n = 1$) fills the narrow space between the two waveguides. This procedure is valid when the mode is well confined and when the index in the gap is far from that of the core. It reveals that the coupling length is divided by 2.5 when the air is replaced by water ($n = 1.33$), and by 3.5 when a matching index fluid ($n = 1.4$) is used. One may be concerned with the power loss due to the out-of-plane bending of the waveguide that can be observed in Fig. 3. However, we should take care of the largely exaggerated vertical scale of the graph. An estimate of the radius of curvature of the waveguide, R , is obtained by considering that the beam profile is described by two arc of a circle of length $L/2$ with a horizontal tangent at one end that are jointed together. Then, neglecting the shortening of the beam due to the bending, we may use the Pythagore's theorem in the triangle with side R , $R - (g/2)$ and $L/2$ and we find

$$R \approx \frac{L^2 + g^2}{4g} \quad (4)$$

where L is the length of the bending arm and g the width of the gap between the two waveguides. For typical structure, $L = 200 \mu\text{m}$ and $g = 4 \mu\text{m}$, yielding a radius of curvature $R = 2.5 \text{ mm}$. In regard of the relatively large index difference along the vertical direction in the waveguide, the total expected bending losses are below 0.05 dB for the rib and the strip-loaded waveguides [16].

B. Attenuator/Polarizer

If we replace the bending waveguide with an absorbing material that may dip in the evanescent field of the lower waveguide, the device becomes an optical attenuator. As will be described latter, the attenuation may depend or not on the state of polarization of the light. The decrease of light power with distance is expressed by

$$I(z) = I(0)e^{-\alpha z} \quad (5)$$

where α is the intensity attenuation factor. This constant is proportional to the imaginary index of refraction of the absorbing medium and to the overlap of the optical field with

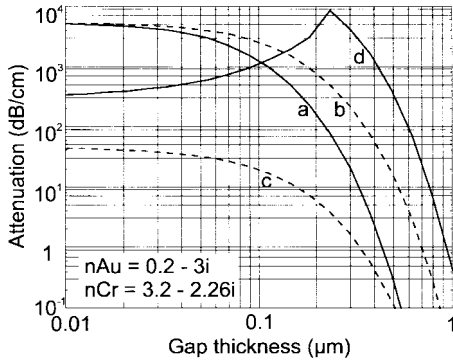


Fig. 5. Attenuation in a SiON rib waveguide coupled with an absorbing material through a low-index substance at $\lambda = 0.633 \mu\text{m}$. Attenuation for (a) the TE mode with chromium and air in the gap, (b) the TE mode with chromium and water ($n = 1.31$) in the gap, (c) the TE mode with gold and water in the gap and, (d) the TM mode with gold and water in the gap.

this medium. Using the effective index method we compute the imaginary and real parts of the propagation constant. We solve the resonant equation in the two orthogonal planar waveguides by a numerical method. The equivalent planar vertical waveguide is a four-layer structure with an absorbing medium. The eigenvalue equation is complex and is very cumbersome to solve. Therefore, we have used an approximate solution rederiving the relations of the perturbation method proposed by She [17]. Fig. 5 shows the optical attenuation for the TE and TM modes in the SiON rib waveguide when the gap width is varied. Three different configurations with different absorbing materials and different substances in the gap (air or water) are presented.

It is evident from Fig. 5 that the materials behave differently whether they have a negative real part of permittivity (e.g., gold where $\epsilon_r = n^2 = -10.3 + 1.0i$) or not (e.g., chromium where $\epsilon_r = n^2 = 5.07 + 14.9i$). In the first case, for specific gap values, the TM modes excite surface plasmon and present much higher loss than the TE modes [Fig. 5(c) and (d)]. This condition emphasizes the polarizing behavior of the device. In order to get a compact attenuator, with the highest possible coefficient of absorption, we have to use a material having a positive real part of permittivity. For the same substance in the gap, they present higher loss and less dependence with polarization than the former materials [Fig. 5(b) and (c)] although this dependence may still amount to half an order of magnitude. In this later case, attenuation as large as 100 dB/cm may be obtained with the rib waveguides for TE polarization (50 dB/cm for TM polarization) even if the substance in the gap is the air [Fig. 5(a)]. This model may also be used to estimate the thickness of the buffer-layer that is needed to avoid excessive loss in the waveguide. Considering the attenuation experienced by visible light ($\lambda = 0.633 \mu\text{m}$) in single-crystal silicon ($n = 3.85 - 0.02i$), a 2.5- μm -thick SiO₂ layer under the waveguide keeps the loss below 0.1 dB/cm.

IV. MECHANICAL MODEL

The design of the actuator relies heavily on the optical design. The main relevant points are summarized below.

- A displacement of 1 μm of the waveguide is sufficient to obtain the coupled and uncoupled states of the device,

- in crossover state the gap between the waveguides should be as small as possible for achieving short device length,
- an SiO₂ 2.5- μm -thick buffer-layer should be inserted between the waveguide core and the silicon substrate to avoid excessive loss at the wavelength of 0.633 μm .

With these points in mind, we choose the short range and powerful electrostatic actuation. Planar electrodes will be placed aside the two waveguides. The upper bending structure will be made of two thin arms supporting a rectangular plate for the electrodes. This structure will also be crossed by the upper waveguide. The behavior of a planar electrostatic actuator with a restoring spring is well known [18]. Neglecting fringing effects, the equilibrium's equation between the electrical and mechanical forces is expressed as

$$x^3 - x_0x^2 + \frac{S}{K} \frac{\epsilon_0\epsilon_r}{2} V^2 = 0 \quad (6)$$

where x_0 is the initial width of the gap between the electrodes, ϵ_0 the vacuum permittivity, ϵ_r the relative permittivity of the substance filling the gap between the electrodes, K the restoring spring constant, S the planar electrodes surface, and V the voltage between the electrodes. The solution of (6) gives the width of the gap according to the voltage. We used the trigonometric method to solve the third-order equation and ignoring the nonphysical roots ($x \geq 0$), we obtain

$$x = \begin{cases} \frac{2}{3}x_0 \cos \left[\frac{1}{3} \arccos \left(1 - \frac{2V^2}{V_P^2} \right) \right] + \frac{x_0}{3} \\ \frac{2}{3}x_0 \cos \left[\frac{1}{3} \arccos \left(1 - \frac{2V^2}{V_P^2} \right) + \frac{4\pi}{3} \right] + \frac{x_0}{3}, & V \leq V_P \\ 0, & V > V_P. \end{cases} \quad (7)$$

This solution reveals a snapping effect that is used for two-state actuation. When the voltage excess V_P , the pull-in voltage, the movable electrodes goes inexorably toward the counter electrodes. Thus, a proportional command is possible only in the range 0 to V_P . In this range, the equation has two roots, but the first solution given in (7), for a gap varying between x_0 and $(2/3)x_0$, is the only one that is physically stable as can be seen by looking at the sign of the derivative (i.e., the gap should decrease when the voltage is increased). The pull-in voltage is fundamental to the actuator design and is given by

$$V_P = 1.83 \cdot 10^5 x_0^{3/2} \sqrt{\frac{K}{\epsilon_r S}}. \quad (8)$$

Actually, if we define the insulated electrodes in the same plane as the waveguides, the snapping effects will insure a very tight contact between the waveguides. Moreover, if we use recessed electrodes, as shown in Fig. 6, we may obtain displacement proportional to the applied voltage in the whole gap at the expense of a sixfold increase in the operating voltage.

Simulating the bending structure with FEM (ANSYS) allows relating its dimensions with its stiffness. Using (8), we further relate the stiffness of the actuator to the operating

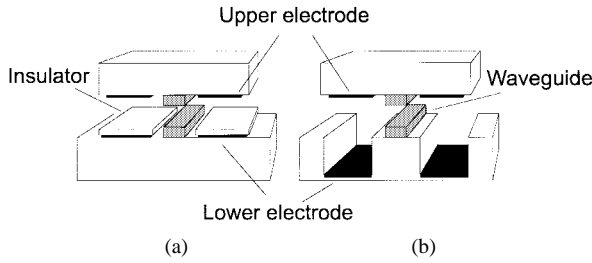


Fig. 6. (a) ON/OFF snapping actuator with insulated electrodes and (b) proportional actuator with recessed electrodes.

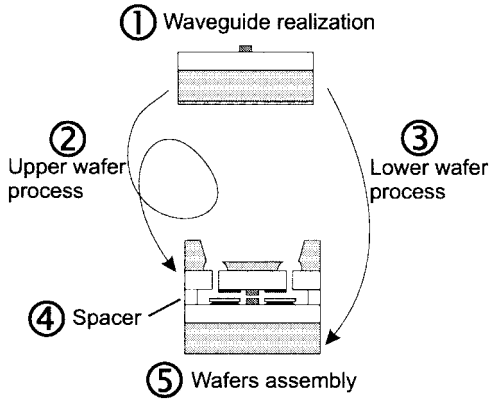


Fig. 7. Two wafers process for optical coupler on silicon.

voltage. For two $15\text{-}\mu\text{m}$ -wide and $200\text{-}\mu\text{m}$ -long bending arms ($K = 5\text{ N/m}$), a $4\text{-}\mu\text{m}$ -thick air-gap ($\epsilon_r = 1$), and $200\text{ }\mu\text{m} \times 200\text{ }\mu\text{m}$ electrodes, the snapping voltage is kept under 20 V . The thickness of the SiO_2 mechanical structure, and hence of the arms, is fixed by previous optical consideration and is $2.5\text{ }\mu\text{m}$. In that case, taking into account the presence of an SiO_2 -insulating layer $0.5\text{ }\mu\text{m}$ thick between the electrodes, the contact force is 1 mN , more than 50 times the restoring spring force. Eventually, we know the main feature of the device and will address in the next paragraph the fabrication sequence with the presentation of some realized devices.

V. FABRICATION

The device is based on the assembly of two wafers, a lower wafer with a waveguide and insulated or recessed electrodes and an upper wafer with a bending waveguide and its coplanar electrodes. The two wafers are then aligned and bonded together. Finally, the wire bonding of the electrodes complete the device. The general flow of this process is shown in Fig. 7.

The main challenge of this process is the realization of the upper wafer with the bending waveguide. A more detailed process of the upper wafer is presented in Fig. 8.

The process starts with the realization of the waveguides [Fig. 8(a)]. We etch $1.5\text{-}\mu\text{m}$ -wide stripe out of a $0.8\text{-}\mu\text{m}$ -thick LPCVD SiON layer ($n = 1.510$ [19]) deposited on top of the $2.5\text{-}\mu\text{m}$ -thick SiO_2 buffer layer ($n = 1.454$). Then we etch the wafer from the backside in a 33%-KOH solution through a SiN -mask. With a two-steps etch we obtain simultaneously a pit with a $20\text{--}30\text{-}\mu\text{m}$ -thick silicon bottom and through-the-wafer holes for electrical connections [Fig. 8(b)]. The etch-stop is controlled by an original optical stop technique

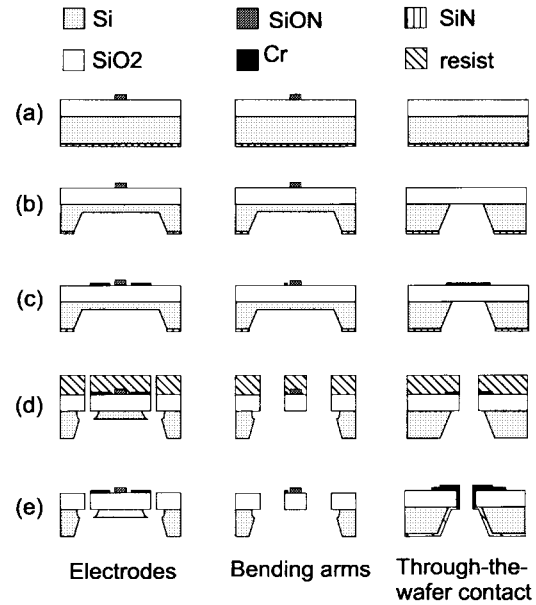
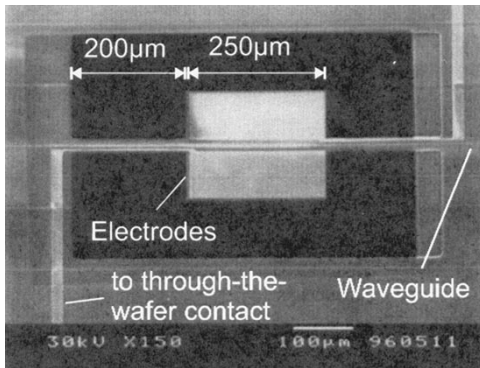


Fig. 8. Process for the upper wafer. The columns show the process along different cut of the wafer: (left) the electrode support, (middle) the bending arm, (right) the hole through the wafer that brings the electrode contact to the back of the wafer.

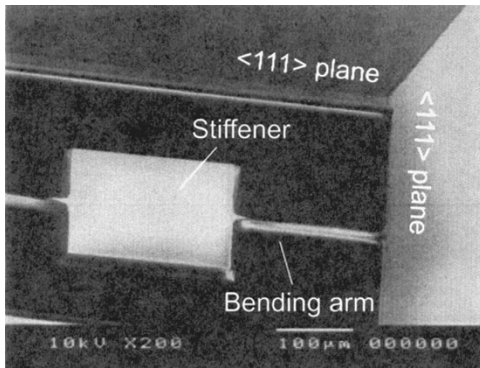
that will be described elsewhere. The thick layer of single crystal silicon is kept under the electrodes to lower the warping of the surface due to stress gradient inside the deposited layers. The upper chromium electrodes are then deposited and patterned near the waveguide [Fig. 8(c)]. We pattern with RIE (CHF_3 , 13 mT , 200 W) through a thick-resist mask the SiO_2 -layer and the remaining silicon to free the mechanical structure. We use RIE isotropic etching of silicon (SF_6 , 100 mT , 100 W) to remove the silicon from the bending arms, thus reducing their stiffness, while keeping a thick layer behind the electrodes, to maintain them flat [Fig. 8(d)]. The evaporation through a shadow mask of a Cr-Au layer on both sides of the wafer creates a ground plane on wafer back that connects through the wafer with all the bending structure electrodes [Fig. 8(e)]. Fig. 9 shows the front and backside of the upper wafer with the outgoing contacts and the waveguide running on the thin bending arms.

For the lower wafer we start with the patterned waveguide and evaporate chromium on the whole wafer. Then, we lift off a $0.5\text{ }\mu\text{m}$ thick sputtered SiO_2 layer using thick photo-resist to provide the insulator pattern. This step is followed by the wet etch of the metallic layer while protecting the contact pad of the electrodes with photoresist. This layer is slightly over-etched to obtain the insulated electrodes with an auto-aligned process. The deposition of a spacer layer (using photoresist or lifted off SiO_2) completes the realization of the lower wafer (Fig. 10).

Eventually the upper wafer is flipped and is placed, with the lower wafer, in a 6-DOF positioning tool with a 20-nm pitch mounted on a vibration-absorbing base. The alignment is made possible by the absence of silicon on the bending arms that allows viewing the waveguides from the backside with the microscope objective (X1000) of a probe-station. The alignment accuracy is estimated to be better than $0.5\text{ }\mu\text{m}$. The



(a)



(b)

Fig. 9. Front side and backside SEM view of the upper wafer with the bending waveguide. Remark the thick layer of single-crystal silicon on the rectangular electrodes back.

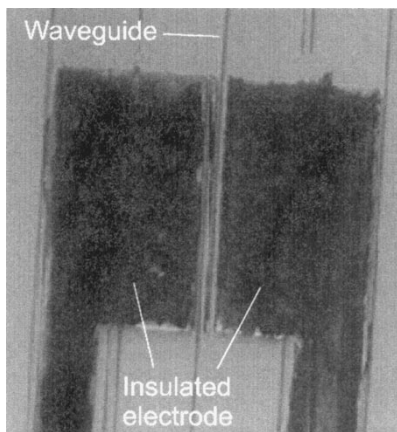


Fig. 10. Microphotograph of the lower wafer with the waveguide running between the insulated electrodes.

two chips are then firmly clamped until complete drying of the epoxy applied on the wafer edge. Finally, wire bonding with gold is performed to connect the upper electrodes ground plane and the lower electrodes contacts to the pins of a DIL package. Fig. 11 presents a photograph (scale $\times 2$) of a device mounted on a modified IC DIL connector.

VI. EXPERIMENT

The snapping voltage was between 40–85 V with $200 \mu\text{m} \times 200 \mu\text{m}$ electrodes and $200 \mu\text{m} \times 18 \mu\text{m} \times 2.5 \mu\text{m}$ SiO_2

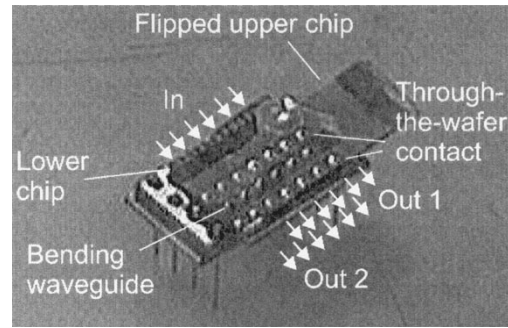


Fig. 11. 6 MEOMS coupler on a chip carrier.

bending arms. This is a 2–4 times increase from the model prediction that neglects the presence of the insulating layer on the lower electrodes. This discrepancy may be further explained by the compressive stress inside the layer that stiffens the bending structure. Moreover, the bulging of the suspended structure or the warping of the wafer submitted to a gradient of stress does not allow to obtain a perfect parallelism between the two wafers. This effect tends to increase the initial gap width from the designed $4 \mu\text{m}$ to 5–6 μm . The cutoff frequency of the actuator is below 1 kHz with no measurable resonance. This is consistent with the large damping experienced by the actuator from the squeezed air film between the electrodes. Thus the maximum switching speed of the device is around 1 ms. Etching holes in the support of the upper electrodes to reduce the damping will slightly improve this figure. For the optical test of the device we couple the light of a collimated 630-nm LD into the waveguide using microscope objective and we observe the magnified output plane with a CCD camera. Rotation of the LD source and a cube polarizer are used to select between the TE and TM modes. The waveguide appears to be single mode with an elliptical mode measuring $2 \mu\text{m} \times 1 \mu\text{m}$. For such a small size, coupling the light from the LD to the waveguide is performed with a very low efficiency and the estimated loss were above 10 dB. In order to avoid high loss when coupling the waveguide to a fiber optic, tapered waveguides should be used at the input and output port of the device. The optical loss is measured using a derivation of the cut-back technique. A mean value of $12 \text{ dB} \pm 6 \text{ dB/cm}$ was revealed by our measurements, with TM modes regularly presenting higher loss than TE modes (about 2 dB/cm difference). This large figure is mainly attributed to the scattering loss that appears at the guide boundaries. Actually, they present a large roughness due to the nonoptimized RIE etching at that small dimensions. Strip-loaded waveguides were also fabricated within the same environment and they presented loss of a few decibels per centimeter [20], confirming the hypothesis of loss through scattering at the rough air-core interface, which presents a large index difference in the rib waveguide. In order to test the device as an attenuator the upper waveguide is replaced by a chromium layer 200 nm thick. Then we observe the output plane of the device in the OFF and ON states when light in the TE polarization is launched in the lower waveguide. The additional loss induced by the chromium-layer is -2.3 dB for the 350- μm -long section of chromium considered in Fig. 12.

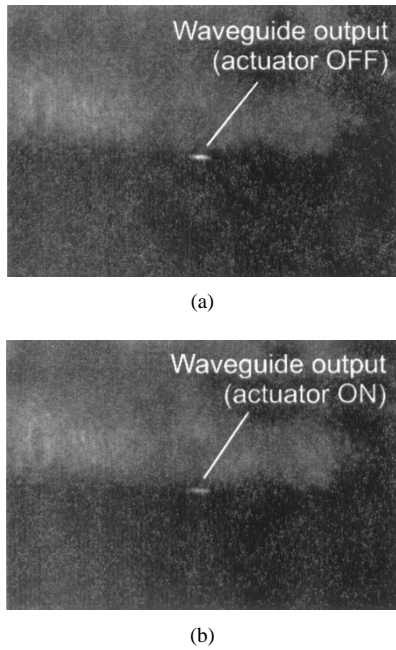


Fig. 12. Attenuator output in (up) OFF and (down) ON states for TE polarization.

This is -65 ± 15 dB/cm, using an estimated error of $\pm 10\%$ on the measurement of the light intensity with the CCD camera (mostly related to the source stability). Higher loss figures are obtained with longer attenuation section. The loss observed with TM polarization was smaller roughly by a factor of two but could not be accurately determined because of the large uncertainty in the measurements. Previous results [21] reported a complete independence on the polarization but they were plagued by an error in the normalization of all the field with the TE mode in the OFF state that experienced less loss than the TM mode.

The value of the attenuation gives a good insight on the gap thickness existing in the actuated state. If we refer to the curve (a) in Fig. 5, we may deduce that the gap is around $0.25 \mu\text{m}$. This value compares well with the roughness measurement we reported previously ($0.1 \mu\text{m}$). It is worth noting that if a film of water exists on the surfaces in contact, the real gap should be larger by a factor of 2. For such a gap, the model of the coupler (Fig. 3) predicts that the coupling length L_C of the device is about $300 \mu\text{m}$. However, when we operated the device, even if the lower waveguide seemed perturbed by the presence of the upper waveguide, no light could be measured at the upper waveguide exit. Even when we increased the coupling length to $350 \mu\text{m}$ and introduced DI-water as a matching index fluid, we did not clearly observe the coupling. The reason seems to stem in the waveguide quality. Actually, in a rib waveguide the propagation constant is very sensitive to the waveguide dimensions. Thus, any width difference between the two waveguides creates a phase mismatch ($\delta \neq 0$) and lowers the coupling as expressed by (1). The maximum exchanged power is then reduced by $1 + (\delta/\kappa)^2$, where δ is half the difference between the propagation constants of the TE- or TM-modes of the two waveguides. In order to relax the constraint on the waveguide realization, future version

of the device will use an inverse-rib waveguide instead of the rib waveguide. The lateral confinement is here obtained with a smaller index difference reducing the influence of the waveguide width on the propagation constant and also reducing the loss by scattering. Other improvements in the waveguide process are awaited to reduce the surface roughness to achieve even shorter devices.

VII. CONCLUSION

We have presented a microelectrooptomechanical system that can be used as a 2×2 optical switch or an attenuator. In this last case we have realized a device exhibiting an attenuation of 65 dB/cm for TE polarization. Using an absorbing material with the negative real part of permittivity (e.g., gold) and a matching index substance we can obtain a controllable polarizer by increasing greatly the loss of the TM mode through the excitation of metallic surface plasmon (Fig. 5). Because of the poor quality of the waveguides, the coupling between the two waveguides has not been clearly established. However, the result obtained with the attenuator seems to indicate that a coupling length in the order of $300 \mu\text{m}$ may be achieved. This very short length will allow for the fabrication of small 2×2 switch ($1 \text{ mm} \times 200 \mu\text{m}$, including the length of the bending arms), suitable for the integration in a large commutation matrix. Apart from the change in the waveguide process, other improvements are envisaged to reduce the time for the alignment by using self-aligning structures deposited on both wafers [22]. This step is essential to achieve efficient packaging, which remains the weak point of many MOEMS devices.

ACKNOWLEDGMENT

The authors want to thank all the members of the Fujita Laboratory for their help during this work and the members of the LPMO for their support during the redaction. They are also indebted to the thoughtful remarks given by anonymous visitors at the MEMS'98 Conference and to L. Han for rereading.

REFERENCES

- [1] J. Mohr, M. Kohl, and W. Menz, "Micro optical switching by electrostatic linear actuator with large displacement," in *Proc. 7th Int. Conf. Solid-State Sens. and Actuat. (TRANSDUCERS'93)*, 1993, pp. 120–123.
- [2] H. Toshiyoshi and H. Fujita, "Electrostatic micro torsion mirrors for an optical switch matrix," *IEEE J. Microelectromech. Syst.*, vol. 5, pp. 231–237, 1996.
- [3] S. Nagaoka, "Compact latching type PANDA fiber switch," *IEEE Photon. Technol. Lett.*, vol. 10, pp. 233–234, Feb. 1998.
- [4] K. Hogari and T. Matsumoto, "Electrostatically driven micromechanical 2×2 optical switch," *Appl. Opt.*, vol. 30, no. 10, pp. 1253–1257, 1991.
- [5] T. Kanai, A. Nagayama, S. Inagaki, and K. Sasakura, "Automated optical main distributing-frame system," in *Tech. Dig. OFC/IOOC*, June 1993, vol. 1, pp. 74–75.
- [6] E. Ollier, P. Labeye, and F. Revol, "Micro-opto mechanical switch integrated on silicon," *Electron. Lett.*, vol. 31, no. 23, pp. 2003–2005, 1995.
- [7] D. Kobayashi, H. Okano, M. Horie, H. Otsuki, K. Sato, and M. Horino, "PLC-based micromechanical optical switch with magnetic drive," in *Tech. Dig. Int. Conf. Optical MEMS and their Applications (MOEMS'97)*, IEEE, 1997, pp. 243–246.
- [8] P. Pliska and W. Lukosz, "Electrostatically actuated integrated optical nanomechanical devices," in *Integrated Optics and Microstructures*, SPIE, vol. 1793, pp. 259–272, 1992.

- [9] G. Magel, "Integrated optic devices using micromachined metal membrane," in *Integrated Optics and Microstructures III*, SPIE, vol. 2686, pp. 54–63, 1996.
- [10] Y. Kim, M. Allen, and N. Hartman, "Micromechanically based integrated optic modulators and switches," in *Integrated Optics and Microstructures*, SPIE, vol. 1793, pp. 183–189, 1992.
- [11] W. Lukosz and P. Pliska, "Integrated optical nanomechanical light modulators and microphones," *Sensors Mater.*, vol. 3, no. 7, pp. 266–280, 1992.
- [12] A. Yariv, "Coupled-mode theory for guided-wave optics," *IEEE J. Quantum Electron.*, vol. 9, pp. 919–933, 1973.
- [13] E. Pennings, R. Deri, A. Scherer, R. Bhat, T. Hayes, N. Andreadakis, M. Smit, L. Soldano, and R. Hawkins, "Ultracompact, low-loss directional couplers on InP based on self-imaging by multimode interference," *Appl. Phys. Lett.*, vol. 59, pp. 1926–1928, Oct. 1991.
- [14] W. Jones, in *Roark's Formulas for Stress & Strain*, 6th ed. Singapore: McGraw-Hill, 1989, ch. 7, p. 100.
- [15] M. MacHenry and D. Chang, "Coupled mode theory of two nonparallel dielectric waveguides," *IEEE Trans. Microwave Theory Tech.*, vol. MTT-32, pp. 1469–1475, Nov. 1984.
- [16] D. Marcuse, *Light Transmission Optics*, 2nd ed. New York: Van Nostrand, 1982, ch. 9, pp. 407–414.
- [17] S. She, "Accurate perturbation analysis of metal-clad and absorptive multilayer dielectric waveguides in near cutoff," *Opt. Commun.*, vol. 135, pp. 241–246, 1997.
- [18] H. Nathanson and R. Wickstrom, "A resonant-gate silicon surface transistor with high- q bandpass properties," *Appl. Phys. Lett.*, vol. 7, p. 84, 1965.
- [19] F. Chollet, M. de Labachellerie, and H. Fujita, "Microoptomechanical devices: An electrostatically actuated bending waveguide for optical coupling," in *Micro-Optical Technologies for Measurement, Sensors, and Microsystems*, SPIE, 1996, vol. 2783, pp. 163–173.
- [20] C. Gorecki, F. Chollet, E. Bonnotte, and H. Kawakatsu, "Silicon-based integrated interferometer with phase modulation driven by surface acoustic waves," *Opt. Lett.*, vol. 22, no. 23, pp. 1784–1786, 1997.
- [21] F. Chollet, M. de Labachellerie, and H. Fujita, "Electromechanically actuated evanescent optical switch and polarization independent attenuator," in *Proc. 11th Annu. Int. Workshop Micro Electro Mechanical Systems (MEMS'98)*, IEEE, 1998, pp. 476–481.
- [22] B. Acklin, J. Bellerman, M. Schienle, L. Stoll, M. Honsberg, and G. Muller, "Self-aligned packaging of an optical switch array with integrated tapers," *IEEE Photon. Technol. Lett.*, vol. 7, pp. 406–408, Apr. 1995.

Franck Chollet received the electronics engineering degree from the EN-SERB, Bordeaux, France, in 1991, and the doctorate degree in Sciences Pour l'Ingénieur from the Université de Franche-Comté, Besançon, France, in 1995, for his work on integrated optics devices for the CNET (France Telecom). He was then with LIMMS, a French–Japanese laboratory, for two years, hosted by H. Fujita at the IIS, University of Tokyo, Tokyo, Japan, as a JSPS Post-Doctoral Fellow, where he developed optical MEMS. After a short stay at LPMO, Besançon, France, he became a Research Associate at the IMRE, Singapore, where he works on MEMS optical sensors and switches.

M. de Labachellerie, photograph and biography not available at the time of publication.

Hiroyuki Fujita (S'76–M'80), for photograph and biography, see this issue, p. 3.